Chemical Science

ROYAL SOCIETY OF CHEMISTRY

EDGE ARTICLE

View Article Online
View Journal

Cite this: DOI: 10.1039/d6sc01014h

All publication charges for this article have been paid for by the Royal Society of Chemistry

Unveiling the role of local temperature gradients in individual zeolites containing metal active sites

Bing Zhao,[ab] Zhikang Xu,[e] Guida Li,[ab] Gang Meng,[a] Hang Chen,[b] Tong Zhao,[f] Haibo Zhu,[d] Dan Zhao,[b] Mingbin Gao,*[c] Mao Ye*[ab] and Zhongmin Liu[b]

The spatial distribution of active sites governs the behavior of solid catalysts, yet how it shapes local temperature gradients and thereby affects catalytic performance remains poorly understood. Here, using the industrially important propane dehydrogenation (PDH) over CoO_x confined in silicalite-1 (S-1) zeolites as a model system, we show that catalytic activity and stability are enhanced when CoO_x is peripherally confined near the crystal surface (CoO_x@S-1-M), rather than uniformly distributed throughout the zeolite (CoO_x@S-1-U), which differs from conventional catalyst design strategies that emphasize uniform active-site dispersion for stability. To uncover the origin of this behavior, we probe the local temperatures of CoO_x clusters by developing *in situ* high-resolution microscopic Raman thermometry. CoO_x@S-1-U exhibits a pronounced core-to-edge thermal gradient, with the temperature difference exceeding 17 °C, whereas CoO_x@S-1-M maintains a much more uniform temperature distribution, with the difference limited to 8 °C. CoO_x@S-1-M also exhibits higher propane conversion and stability, consistent with this thermal behavior. Mechanistic analysis reveals that the smaller temperature drop at CoO_x clusters in CoO_x@S-1-M enhances propylene desorption and suppresses side reactions and coke formation, deviating from the commonly accepted view that higher temperatures generally promote coke growth. These findings establish a direct link between active-site spatial location and catalytic performance through microscale temperature gradients at active clusters, providing a new perspective for the rational design of supported metal catalysts.

Received 4th February 2026
Accepted 14th May 2026

DOI: 10.1039/d6sc01014h

rsc.li/chemical-science

1. Introduction

Confinement of metal active sites within zeolites has demonstrated significant potential in developing catalysts with enhanced activity, selectivity, and stability for industrially relevant processes, including dehydrogenation/hydrogenation and oxidation.[1–4] These zeolite-supported metal catalysts combine the intrinsic structural stability and confined microenvironments of zeolite frameworks, demonstrating superior performance in the catalytic conversion of energy-relevant small molecules.[5–8] Extensive efforts have been devoted to the precise design of the structure and coordination of metal catalysts within confined nanochannels. Notably, even when the metal loading, structure, and coordination remain constant, the spatial distribution of metal species within the zeolite support can play an equally critical role in determining catalytic performance.[9] By precisely controlling the spatial positioning of active sites, the activity and product selectivity of zeolite-catalyzed reactions can be effectively modulated.[10–12] Investigating the spatial distribution of active sites is essential for comprehensively characterizing the intrinsic properties of catalysts and for the rational design and optimization of zeolite-supported metal catalysts.[13]

Zeolite-supported catalysts are known to exhibit heterogeneous spatial distributions of active sites,[14–19] which can lead to nonuniform reaction rates within zeolite during exothermic or endothermic processes. This, in turn, gives rise to site-specific temperature variations and spatial thermal gradients.[20] The localized thermal fluctuations have a direct impact on macroscopic catalytic activity and stability,[21,22] particularly in zeolite-supported metal catalysts where metal active sites often exhibit spatial segregation.[23–25] This effect becomes pronounced in highly endothermic and industrially important reactions, such as the propane dehydrogenation (PDH) reaction.[26–29] These challenges call for the development of spatially resolved thermometric techniques capable of mapping local thermal environments at active sites.

However, *in situ* thermometry inside individual catalysts is a fundamental yet non-trivial task. Few characterization

[a]Department of Chemical Physics, University of Science and Technology of China, Hefei, Anhui, China, 230026. E-mail: maoye@dicp.ac.cn
[b]Dalian Institute of Chemical Physics, Chinese Academy of Sciences, Dalian, Liaoning, China, 116023
[c]Department of Chemical and Biochemical Engineering, College of Chemistry and Chemical Engineering, State Key Laboratory of Physical Chemistry of Solid Surfaces, Xiamen University, Xiamen, Fujian, China, 361005. E-mail: mbgao@xmu.edu.cn
[d]National Engineering Research Center of Chemical Fertilizer Catalyst, School of Chemical Engineering, Fuzhou University, Fuzhou, Fujian, China, 350002
[e]Qingyuan Innovation Laboratory, Quanzhou, China, 362801
[f]Analytical Solution Plaza, HORIBA (China) Trading Co., Shanghai, China, 200335

techniques can directly measure the local temperature of catalysts under reaction conditions. While conventional characterization techniques including IR[30] and nuclear magnetic resonance (NMR) thermometry[31] offer critical insights into the bulk thermal information of catalyst beds, their inherent spatial resolution limitations at the millimeter scale preclude applications for micro- and nano-structured catalysts.[32] Major advancement in the applications of luminescent thermometry has been achieved by Weckhuysen and co-workers,[14,33,34] in which optically responsive probes were incorporated into catalyst matrices for spatially resolved thermal sensing. Recently, Tian *et al.* employed two-photon confocal microscopy combined with up-conversion luminescence[35] to enable temperature mapping within individual catalyst particles during the methanol-to-hydrocarbons reaction. Filez *et al.* successfully applied X-ray absorption fine-structure (XAFS) thermometry to achieve *in situ* temperatures of active Ni nanoparticles.[36] Recent *operando* thermometry studies on propane dehydrogenation have highlighted the critical role of temperature in catalytic activity and deactivation,[37] while also showing that reliable temperature measurement under reaction conditions remains challenging. However, these studies mainly probe catalyst temperature at the particle or bed level, whereas the local temperature of the active phase within confined catalysts remains much less explored. Although thermometric techniques have advanced significantly, accurately probing local thermal variations of active clusters with spatial resolution in catalyst supports remains challenging, especially for zeolite-supported metal catalysts. Luminescence thermometry measures the temperature of the catalyst matrix rather than that of the active clusters and has thus far been applied mainly to industrial-scale catalyst particles rather than individual zeolites. XAFS provides a potential route to obtain the temperature of active nanoparticles, but spatially resolved measurements still require further investigation. Therefore, the development of *in situ* thermometry techniques with spatial resolution for zeolite-supported active clusters is imperative.

Owing to the relationship between Raman shift and temperature, microscopic Raman spectroscopy has shown promise for *in situ* thermometry.[38] In this work, we propose the use of high-resolution microscopic Raman (HR-mRaman) spectroscopy to spatially probe the local temperature of CoO_x clusters supported within silicalite-1 (S-1) during the PDH reaction. By designing two CoO_x@S-1 catalysts with distinct spatial distributions of CoO_x active sites,[39,40] we probe the temperature distribution within individual zeolites under reaction conditions.[41,42] Concurrently, *in situ* Fourier transform microscopic infrared (FT-mIR) spectroscopy and matrix-assisted laser desorption/ionization Fourier transform ion cyclotron resonance mass spectrometry (MALDI FT-ICR MS)-photoluminescence (PL) coupling were employed to track the spatiotemporal evolutions of active-intermediates and coke species within individual zeolites. In parallel, periodic density functional theory (DFT) and molecular dynamics (MD) simulations were performed to elucidate the effect of temperature on coke formation. This multi-modal strategy allowed for a systematic and profound investigation on the effects of spatial distribution of active sites on the catalytic performance, including conversion efficiency and stability, from the perspective of the local heterogeneous thermal environment.

2. Results and discussion

2.1 Characterization of the zeolite-supported metal oxide catalysts

The S-1 support, synthesized by the conventional hydrothermal method, exhibits a uniform size distribution of ~120 μm (Fig. S1). Cobalt oxides (CoO_x), at a loading of ~5 wt%, were incorporated into S-1 (denoted as CoO_x@S-1) by wet-impregnation (denoted as CoO_x@S-1-M, where M means marginal) and an ultrasound-assisted method (denoted as CoO_x@S-1-U, where U means uniform), respectively (for details, see the SI). After high-temperature calcination in an oxidation atmosphere, the spatial distribution of active CoO_x catalysts can be controlled in S-1. X-ray diffraction (XRD) patterns of CoO_x@S-1 (Fig. S2) reveal characteristic peaks at approximately 8.2°, 9.0°, 23.3°, 24.1°, and 24.6°, corresponding to the MFI framework.[43,44] Nitrogen adsorption–desorption isotherms at 77 K (Fig. S3) confirm that the microporous structure of S-1 remained intact after the incorporation of CoO_x. Table S1 presents the loading of Co species in CoO_x@S-1-M and CoO_x@S-1-U, alongside their BET surface area and micropore volume, all of which are largely consistent. In Fig. 1a, the ^{29}Si magic-angle spinning nuclear magnetic resonance (^{29}Si MAS NMR) spectra show a characteristic peak at −116 ppm, which corresponds to the $Si(OSi)_4$ species (Q_4).[43,45] The evident broadening of the −116 ppm resonance in CoO_x@S-1-M and CoO_x@S-1-U, relative to pristine S-1, indicates increased structural disorder around the framework Si sites, thereby providing strong evidence for the coordination of Co species with Si atoms through the formation of Co–O–Si linkages. Fourier transform infrared (FTIR) spectra of CoO_x@S-1 reveal identical characteristic peaks (Fig. S4), with asymmetric stretching vibrations of the Si–O–Si bridge observed around 1090 cm^{-1}.[46,47] And the Co–O–Si band around 1000 cm^{-1} confirms the incorporation of CoO_x into S-1.[48,49]

The coordination state of CoO_x in S-1 is provided in Fig. 1b and c. The normalized X-ray absorption near-edge structure (XANES) spectra of CoO_x@S-1 are similar to Co_2O_3, and the Fourier transform (FT) extended X-ray absorption fine structure (EXAFS) spectra reveal bands at approximately 2.05 Å and 3.04 Å (ref. 50) (corrected distances), which corresponds to Co–O and Co–Co bonds in the first and second shells, respectively (Table S2). Based on the average coordination number (CN) in Co–O of 4.9 and in Co–O–Co of 4.0, CoO_x@S-1 should contain CoO_x clusters, which is supported by the fitting curve of *k*-edge EXAFS (Fig. S5) and the wavelet transform analysis (Fig. S6). The spatial distribution of CoO_x in CoO_x@S-1-M and CoO_x@S-1-U was studied *via* time-of-flight secondary ion mass spectrometry (TOF-SIMS). TOF-SIMS was employed to analyze the spatial distribution of Co ions across each vertical layer from the external surface to the interior of the individual S-1. As shown in Fig. 1d, the Co ion content inside the CoO_x@S-1-M catalyst is significantly lower than that near the external surface, indicating that the CoO_x species are confined within the zeolite but

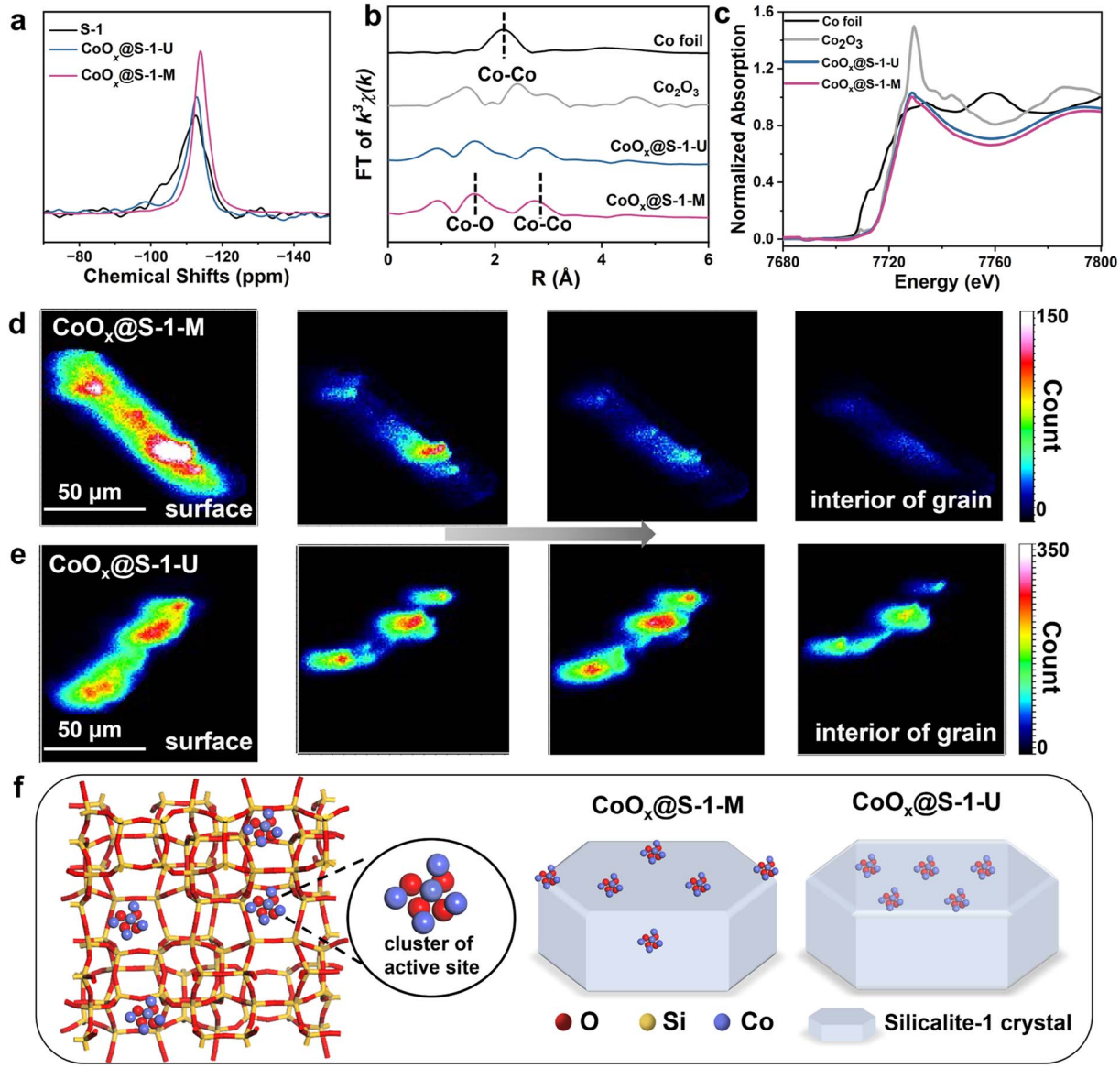

Fig. 1 Characterization of CoO_x@S-1 catalysts and active Co species structures. (a) The ^{29}Si MAS NMR spectra of CoO_x@S-1-M and CoO_x@S-1-U catalysts. (b) Fourier transform k^3-weighted EXAFS spectra and (c) *k*-edge XANES spectra of CoO_x@S-1-M and CoO_x@S-1-U catalysts, compared with reference spectra of Co foil and Co_2O_3. Spatial distribution of CoO_x catalysts within S-1 at different depths determined *via* TOF-SIMS using the mass-to-charge ratio (*m*/*z*) signal of secondary Co ions in the (d) CoO_x@S-1-M and (e) CoO_x@S-1-U catalysts. The images from left to right represent the Co ion concentration across different depths, spanning from the external surface to the interior of the individual zeolite. (f) Schematic diagram of the structure of CoO_x catalysts in S-1 and the spatial distribution of CoO_x in S-1 based on the obtained characterization studies.

predominantly distributed in regions close to the crystal surface. In contrast, Fig. 1e illustrates a uniform distribution of CoO_x throughout the CoO_x@S-1-U catalyst. Fig. 1f confirms that the Co species are coordinated as oxide clusters within the S-1 framework and clearly highlights the distinct spatial distributions of CoO_x clusters in CoO_x@S-1-M and CoO_x@S-1-U.

2.2 Catalytic performance of PDH on CoO_x@S-1 catalysts

Long-term PDH reactions were carried out in a fixed-bed reactor for CoO_x@S-1-M and CoO_x@S-1-U at different temperatures (500, 525, 550, 575, and 600 °C). Fig. 2a and S7 show the continuous decline in propane conversion with time on stream. Notably, at the testing temperature, the conversion over the entire PDH reaction of propane on CoO_x@S-1-M is higher than that on CoO_x@S-1-U. The propane conversion is far below the equilibrium conversion of PDH reactions (Table S3). In addition, the inactivation constant (k_d) of CoO_x@S-1-M and CoO_x@S-1-U was calculated at 575 and 600 °C (where the initial propane conversion is greater than 10%), with the deactivation constant determined as described in the SI on page S9 (Fig. 2b). The slightly higher k_d of CoO_x@S-1-U compared with CoO_x@S-1-M suggests that CoO_x@S-1-M possesses both higher catalytic

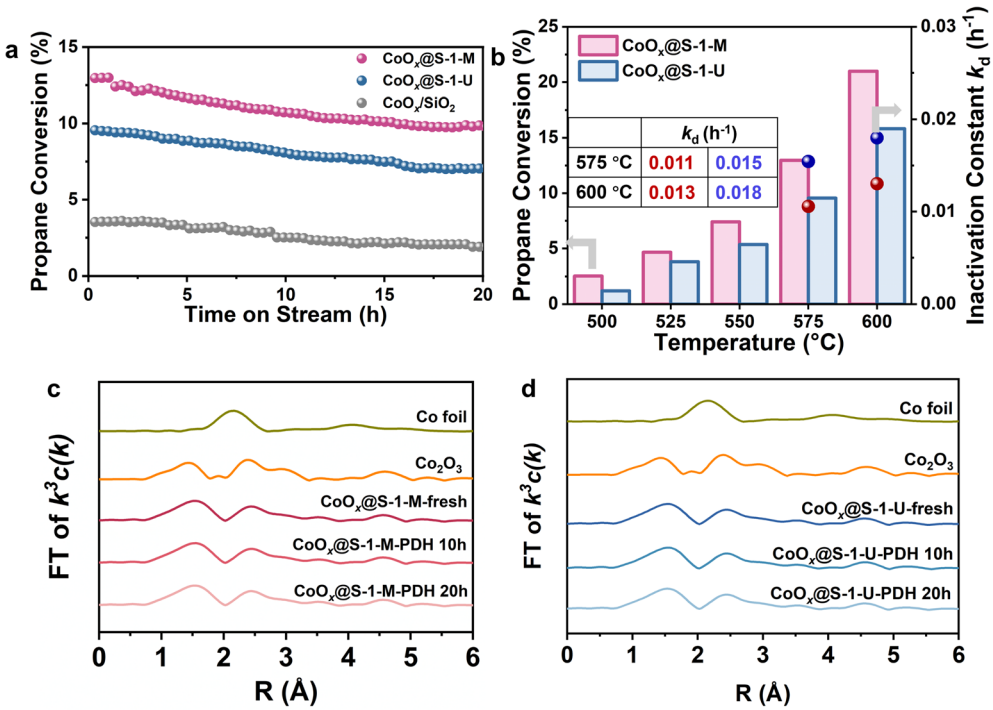

Fig. 2 Catalytic performance of the PDH reaction on CoO_x@S-1 catalysts. (a) Durability of CoO_x@S-1-M, CoO_x@S-1-U and CoO_x/SiO_2 catalysts. Reaction conditions: feed gas of 20% C_3H_8 and 80% N_2; WHSV = 2.16 $g_{C_3H_8}$ $g_{zeo.}^{-1}$ h^{-1}; T = 575 °C. (b) The effect of temperature on C_3H_8 conversion on CoO_x@S-1-M and CoO_x@S-1-U catalysts and inactivation constants. Reaction conditions: feed gas of 20% C_3H_8 and 80% N_2; WHSV = 2.16 $g_{C_3H_8}$ $g_{zeo.}^{-1}$ h^{-1}. Fourier transform k^3-weighted EXAFS spectra of (c) CoO_x@S-1-M and (d) CoO_x@S-1-U catalysts at different times of stream, compared with reference spectra of Co foil and Co_2O_3.

activity and superior stability. Fig. 2a also shows the catalytic performance of the CoO_x/SiO_2 catalyst, in which active Co species are deposited on the silica surface (Co loading 5%, identical to that of CoO_x@S-1-M), during PDH in a fixed-bed reactor. The all-stage propane conversion on CoO_x/SiO_2 (initial propane conversion ~3%) is markedly lower than that on CoO_x@S-1-M, as the CoO_x clusters supported on the silica surface tend to readily aggregate into larger particles, leading to reduced catalytic activity and stability (Fig. S8 and S9). In contrast, the structure of the active CoO_x species confined within the CoO_x@S-1-M crystals remains much more stable due to the spatial confinement effect of the S-1 framework, resulting in superior catalytic performance compared with CoO_x/SiO_2.

The effects of external and internal mass transfer in PDH over CoO_x@S-1-M and CoO_x@S-1-U were systematically examined to evaluate the accessibility of active Co species in CoO_x@S-1-M and CoO_x@S-1-U. Diffusion experiments of propane within CoO_x@S-1-M and CoO_x@S-1-U were conducted at different temperatures (Fig. S10, see the SI for experimental details and data processing). The diffusion activation energy of propane ($E_{a,diff}$) obtained from the experiments was approximately 16.1 kJ mol^{-1}, in good agreement with the MD simulation results (~16.6 kJ mol^{-1}, Table S4). As summarized in Table S5, the Mears' criterion values are far below 0.15 and the Weisz–Prater criterion values are far below 1,[51] confirming that both external and internal mass-transfer resistances are negligible under the PDH reaction conditions. Furthermore, to quantitatively assess the impact of internal diffusion, the effectiveness factor (η) was determined using Thiele modulus analysis.[52] The η values listed in Table S6 are very close to 1.00, indicating that the active Co species in both CoO_x@S-1-M and CoO_x@S-1-U are fully accessible to propane molecules. In addition, *operando* XAFS, X-ray photoelectron spectroscopy (XPS), and *in situ* ultraviolet-visible (UV-vis) spectroscopy were employed to probe the coordination environments and electronic states of the active Co species in CoO_x@S-1-M and CoO_x@S-1-U during the PDH reaction. All characterization studies were conducted under reaction conditions identical to those in the fixed-bed reactor, with a feed gas consisting of 20% C_3H_8 and 80% N_2, a WHSV of 2.16 $g_{C_3H_8}$ $g_{zeo.}^{-1}$ h^{-1}, and the *in situ* cell temperature maintained at 575 °C. The Co K-edge XANES spectra and Fourier transform k^3-weighted EXAFS spectra of CoO_x@S-1-M and CoO_x@S-1-U at different times on stream are shown in Fig. S11 and 2c, d. Both catalysts exhibit characteristic EXAFS bands at approximately 2.05 Å and 3.04 Å (corrected distances), corresponding to Co–O and Co–Co bonds in the first and second coordination shells,[50] respectively, indicating that the active Co species within the S-1 zeolite remain in oxidized states during the PDH reaction. Based on the average coordination numbers (CN) of ~4.9 for Co–O and ~4.0 for Co–O–Co (Table S7), the coordination structure of the active CoO_x clusters is inferred to remain unchanged throughout the catalytic process, consistent with the fitted *k*-edge EXAFS curves (Fig. S12).

The XPS spectra of CoO_x@S-1-M and CoO_x@S-1-U recorded at different times on stream show no significant shift in the Co 2p binding energy or noticeable variation in the Co^{3+}/Co^{2+} ratio, suggesting that the oxidation state and local coordination environment of cobalt remain nearly constant during the PDH reaction (Fig. S13).[53] *In situ* UV-vis spectra provide additional evidence for the chemical and structural stability of the active Co species (Fig. S14). Both CoO_x@S-1-M and CoO_x@S-1-U display two characteristic absorption bands in the range of 450–700 cm^{-1}, attributable to Co incorporated into the MFI framework.[50] Notably, no apparent band shift or emergence of new features associated with other Co coordination environments is observed at different reaction stages, indicating that the local coordination structure of active Co species remains unaltered during PDH. Collectively, the *operando* XAFS, XPS, and *in situ* UV-vis results confirm that the active Co species in CoO_x@S-1-M and CoO_x@S-1-U remain structurally and chemically stable under PDH reactions, thereby excluding the influence of active-site evolution on the catalytic performance differences between the two catalysts. Therefore, the discrepancy of propane conversion between CoO_x@S-1-M and CoO_x@S-1-U can be attributed to the different local temperatures of CoO_x clusters caused by the different spatial distribution of Co species.

Spatially and temporally resolved characterization studies of the temperature distribution within the CoO_x@S-1 catalysts are crucial for understanding the discrepancy in catalytic performance between CoO_x@S-1-M and CoO_x@S-1-U. To achieve this, we employed a spatiotemporal spectroscopic approach, integrating HR-mRaman, FT-mIR, and MALDI FT-ICR MS-PL coupling to monitor the temperature, active-intermediate species, and coke species within individual zeolite catalysts, as illustrated in Fig. 3a. Temperature is known to strongly influence phonon behavior. Consequently, Raman scattering is widely used to probe temperature-induced phenomena such as phase transitions, lattice strain, and thermal expansion.[54] As the temperature increases, variations in the lattice constants along specific crystallographic directions alter the interatomic spacing and phonon frequencies, thereby causing characteristic shifts in the Raman peaks. By exploiting the relationship between temperature and Raman shift, such a method can detect the temperature variations at active metal oxide sites within individual S-1 crystals (Fig. 3b). Through the use of a two-dimensional precise displacement stage, the spatial

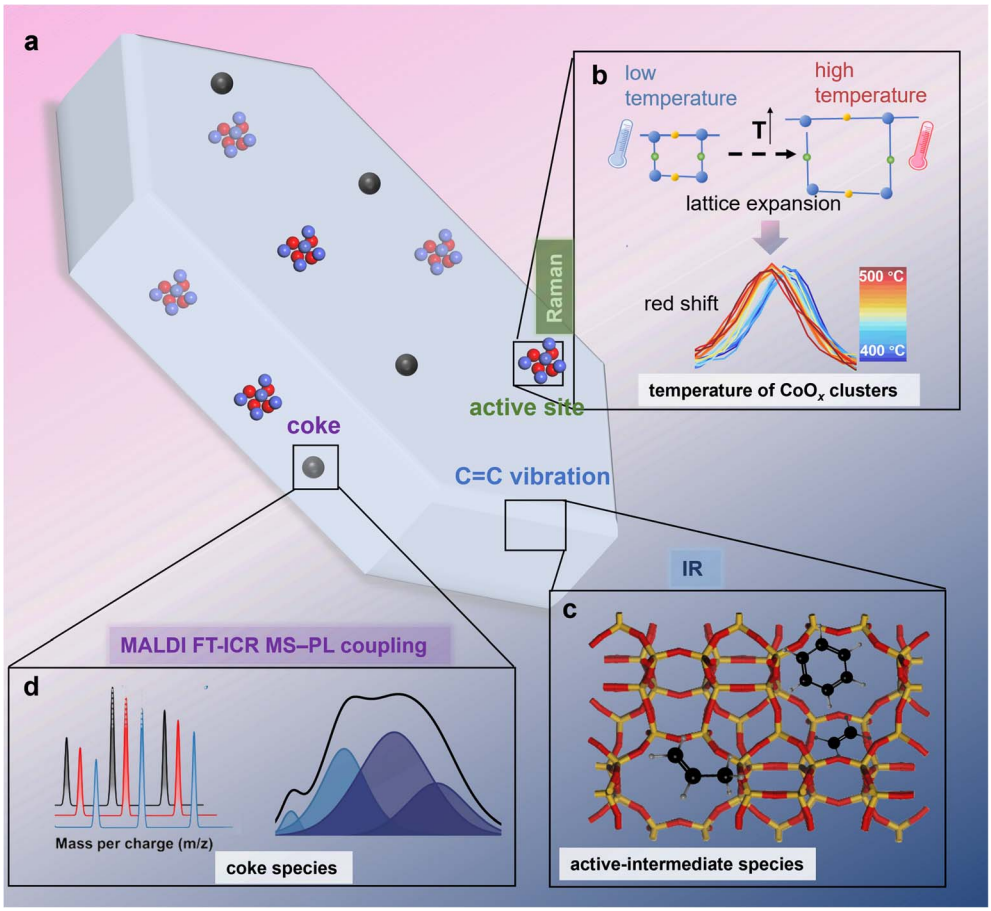

Fig. 3 A schematic of *in situ* spatiotemporally resolved spectroscopy imaging for the investigation of the heterogeneity of individual catalysts. (a) A single crystal of S-1 (blue) incorporated with CoO_x clusters. (b) HR-mRaman for thermometry of active metal oxides, (c) FT-mIR for tracking active-intermediate species, and (d) MALDI FT-ICR MS-PL coupling for the characterization of coke species. Orange, red, and violet spheres represent Si, O, and Co atoms, respectively, while dark gray and white spheres denote C and H atoms.

distribution of temperature at different positions of zeolite can be obtained. Fig. 3c and d illustrate that the spatial distribution of active intermediates within a single catalyst can be identified through FT-mIR with a two-dimensional precise displacement stage, and coke species can be analyzed *via* MALDI FT-ICR MS-PL coupling.

2.3 Non-uniform distribution of local temperatures of active CoO_x clusters within individual zeolites

The discrepancy in catalytic performance between CoO_x@S-1-M and CoO_x@S-1-U catalysts in PDH reactions, despite their identical CoO_x contents, cluster structure and propane diffusion, can be directly attributed to the different spatial distributions of CoO_x. Given that PDH is a highly endothermic reaction and constrained by thermodynamic equilibrium,[39,40] therefore, it is crucial to probe the local temperature within individual crystals. To address this, HR-mRaman was employed to probe the local temperature of active CoO_x clusters at different positions within individual S-1. The Raman spectra of CoO_x@S-1 exhibit a Raman shift at 380 cm^{-1}, which corresponds to Si–O–Si vibration[55,56] and a Raman shift at 690 cm^{-1}, which corresponds to Co–O vibration[57,58] (Fig. 4a). Although the Raman spectrum of CoO_x@S-1 exhibits both the Si–O–Si band (~380 cm^{-1}) and the Co–O band (~690 cm^{-1}), the Si–O–Si vibration is not suitable as a temperature indicator. In silicalite-1, multiple low-frequency framework modes are strongly affected by the polarization of the incident light and crystal orientation, which often leads to peak overlap, shoulder features, and intensity redistribution.[59] As a result, the peak position of the Si–O–Si band cannot be fitted as robustly as that of the Co–O band, making it less reliable for thermometry. Fig. S15 presents Raman spectra acquired by varying typical parameters[13] (*e.g.* exposure time, laser power and scanning cycles). Increasing the exposure time and laser power can effectively enhance spectral intensity and the signal noise ratio, while adding scanning cycles can only improve the signal-to-noise ratio. However, using 50% laser power (40 mW) leads to local laser heating, which causes the local-heating and red-shift of the Raman peak. To minimize laser heating effects during Raman thermometry, a series measured parameters of Raman spectra were attempted, and the optimal parameters were determined, *i.e.* 10% laser power (8 mW), exposure times of 20 s and a single scanning cycle.

As shown in Fig. 4b, temperature-dependent Raman spectra were collected at 5 °C intervals from 400 to 500 °C range, which reveal a consistent red-shift in the Co–O vibration Raman peak

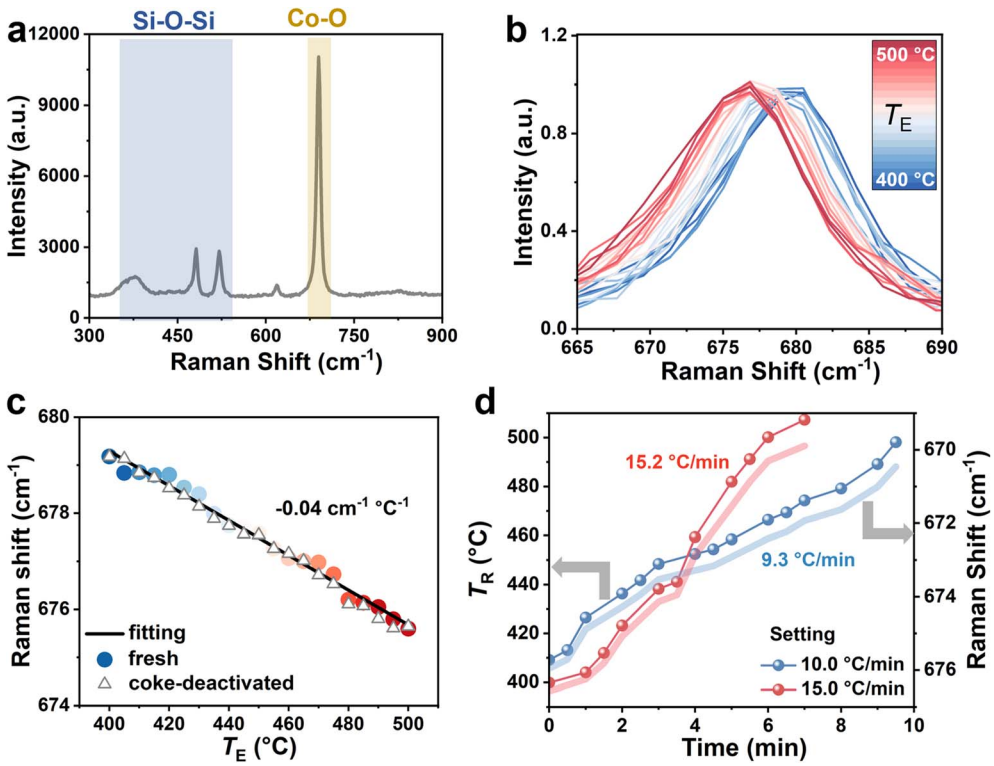

Fig. 4 *In situ* thermometry for metal oxide clusters in zeolites. (a) Raman spectrum of CoO_x@S-1-M recorded at 298 K. (b) Temperature-dependent Raman shift of the Co–O vibration in CoO_x@S-1-M zeolite; spectra were collected from 400 to 500 °C range at 5 °C intervals. The center of the Raman peak was determined by fitting the Raman spectra using a Gaussian function (T_E represents the temperature measured by a thermocouple inside the *in situ* cell). (c) A linear relation was established between Raman shift and temperature, yielding a slope of 0.04 cm^{-1} K^{-1}. And comparisons of the Raman shift between fresh (circle point) and coke-deactivated (triangle point) catalysts are shown. (d) The temperature of active CoO_x clusters from 400 to 500 °C at heating rates of 9.3 °C min^{-1} and 15.2 °C min^{-1}. The temperature was determined from the Raman shift using the linear relationship in (c) (T_R represents the temperature determined by Raman shift). Heating conditions: the *in situ* cell was purged with nitrogen gas at a flow rate of 5 ml min^{-1}. Spectra collection conditions: a 532 nm laser with 8 mW as an excited laser, 20 s exposure time and a single scanning cycle.

with increasing temperature. Here, T_E represents the temperature measured by a thermocouple inside the *in situ* reaction cell. The Raman peaks were fitted to determine their central positions using a Gaussian function. As shown in Fig. S16, the Raman shift at 679 cm^{-1} was plotted as a function of temperature. In Fig. 4c and S17, a linear relationship between the Raman shift of Co–O vibration and temperature is shown, with a slope of -0.04 cm^{-1} ° C^{-1}. These results indicate that the temperature of active CoO_x clusters can be accurately probed using the Raman shift, thereby avoiding the use of complex temperature-indicating factors. The Co–O Raman shift mainly arises from temperature-dependent phonon anharmonicity and thermal expansion.[60] Meanwhile, the Co–O vibrational band is also sensitive to the oxidation state and local coordination structure of Co species. For example, Co(III)–O stretching vibrations are generally observed at higher wavenumbers (~680–690 cm^{-1}), whereas Co(II)–O vibrations typically appear at lower wavenumbers (~600–620 cm^{-1}).[61] Therefore, the reaction atmosphere would affect the Co–O Raman shift only if it induces structural evolution or oxidation-state changes of the active Co species. To exclude this possibility, *in situ* Fourier transform k^3-weighted EXAFS and *in situ* XPS measurements were performed under PDH conditions (Fig. S11–S13). The results confirm that the active Co species in both CoO_x@S-1-M and CoO_x@S-1-U remain structurally and chemically stable during the reaction, indicating that the Raman shift is not affected by reaction-induced changes in the active phase. This demonstrates that the reaction atmosphere does not affect the lattice vibrational frequency through changes in the structure or oxidation state of the active phase, and therefore does not interfere with the temperature–Raman shift calibration. To further examine the robustness of the temperature–Raman shift calibration in PDH-relevant environments, we evaluated the influence of coke deposition and the product-related H_2 atmosphere on Raman thermometry. As shown in Fig. 4c, a linear relationship between Raman shift and temperature can also be obtained for the coke-deactivated sample after 20 h of reaction, which closely matches that of the fresh sample. This result indicates that coke deposition does not change the temperature dependence of the Co–O vibration. In addition, the temperature–Raman shift relationships measured for the fresh sample under N_2 and diluted H_2 atmospheres are in good agreement (Fig. S17d), indicating that the presence of H_2 does not affect the accuracy of the thermometry. Fig. S18 presents the mean and standard deviation of the characteristic peak positions at each temperature across multiple crystals, together with the slope of the temperature–Raman shift linear relationship and its standard deviation. The uncertainty in peak position is in the range of 0.02–0.05 cm^{-1}, corresponding to a temperature uncertainty of $\delta T \approx 0.5$–1.3 °C. This precision is sufficient to resolve the ΔT differences of 10–20 °C observed in this work, thereby confirming the accuracy of the method. To validate its effectiveness in *in situ* monitoring of temperature, *in situ* heating experiments were conducted. As shown in Fig. 4d, Raman spectra were continuously collected from 400 to 500 °C at heating rates of 10.0 °C min^{-1} and 15.0 °C min^{-1}, respectively. By converting the Raman shifts to the temperatures of active CoO_x clusters (denoted as T_R) using the established linear relationship in Fig. 4c, the temperature variations of active CoO_x clusters closely aligned with the programmed heating rates of the *in situ* reaction cell. Such agreement confirms the reliability of Raman thermometry for real-time reaction temperature measurements of the active metal oxide sites. The time-resolved raw Raman spectra (Fig. S19) indicate that reaction-induced optical changes have only a limited influence on the Co–O Raman shift. Although the baseline gradually increases with time on stream, the Co–O band remains sharp throughout the reaction, and the background variation within the fitting window is small. These results confirm that the influence of reaction-induced optical changes on the thermometry results is limited in the present CoO_x@S-1 system. Although such effects can be excluded here, they may still become important in other catalytic systems. Therefore, changes in catalyst optical properties during reaction should be carefully considered when applying optical thermometry under *operando* conditions. The thermocouple in the Linkam CCR1000 cell does not directly contact the crystal, so the absolute crystal temperature may deviate slightly from the set temperature. However, the thermal resistance between the sample and the temperature-sensing region is expected to be small under the present natural-convection conditions, limiting the resulting offset to only a few degrees Celsius. To reduce this uncertainty, Raman spectra were collected and reaction gases were switched only after holding the system at the target temperature for 15 min to allow thermal equilibration. Possible perturbations associated with the flowing gas were further minimized by keeping the *in situ* cell, thermocouple, total flow rate, gas composition, and laser power identical throughout the measurements. More importantly, the key parameter in this work is not the absolute temperature itself, but the relative temperature drop (ΔT) and its spatial distribution within single crystals measured under strictly identical conditions. Under these matched conditions, any systematic offset between the thermocouple reading and the actual sample temperature would not alter the comparative analysis of local temperature gradients. The conclusions therefore arise from relative differences in local thermal response rather than from the absolute accuracy of the external temperature reading. Further improvement of absolute thermometry under reaction conditions will be pursued in future work.

The PDH reaction was carried out by introducing propane gas (flow rate $F = 5$ ml min^{-1} and $T = 575$ °C) into the *in situ* reaction cell (Fig. 5a). Specifically, the *in situ* cell was first stabilized at 575 °C under 100% N_2 flow for 15 min, and the feed was then switched to 20% C_3H_8/80% N_2 (5 ml min^{-1}). In this operation, Raman spectra were continuously collected at the edge, submarginal, and center regions to obtain the evolution of ΔT with time on stream. The first Raman spectrum collected after switching the feed gas was defined as $t = 0$ s at reaction onset. Fig. 5b presents a HR-mRaman bright-field image of the individual catalyst crystal, clearly identifying a single CoO_x@S-1 crystal within the field of view. Using the established linear correlation between Raman shift and temperature, the temperatures of active CoO_x clusters in different locations (edge, submarginal and center position) within the single crystal during the PDH reaction were determined. Fig. 5c illustrates the temperature variations of active CoO_x clusters

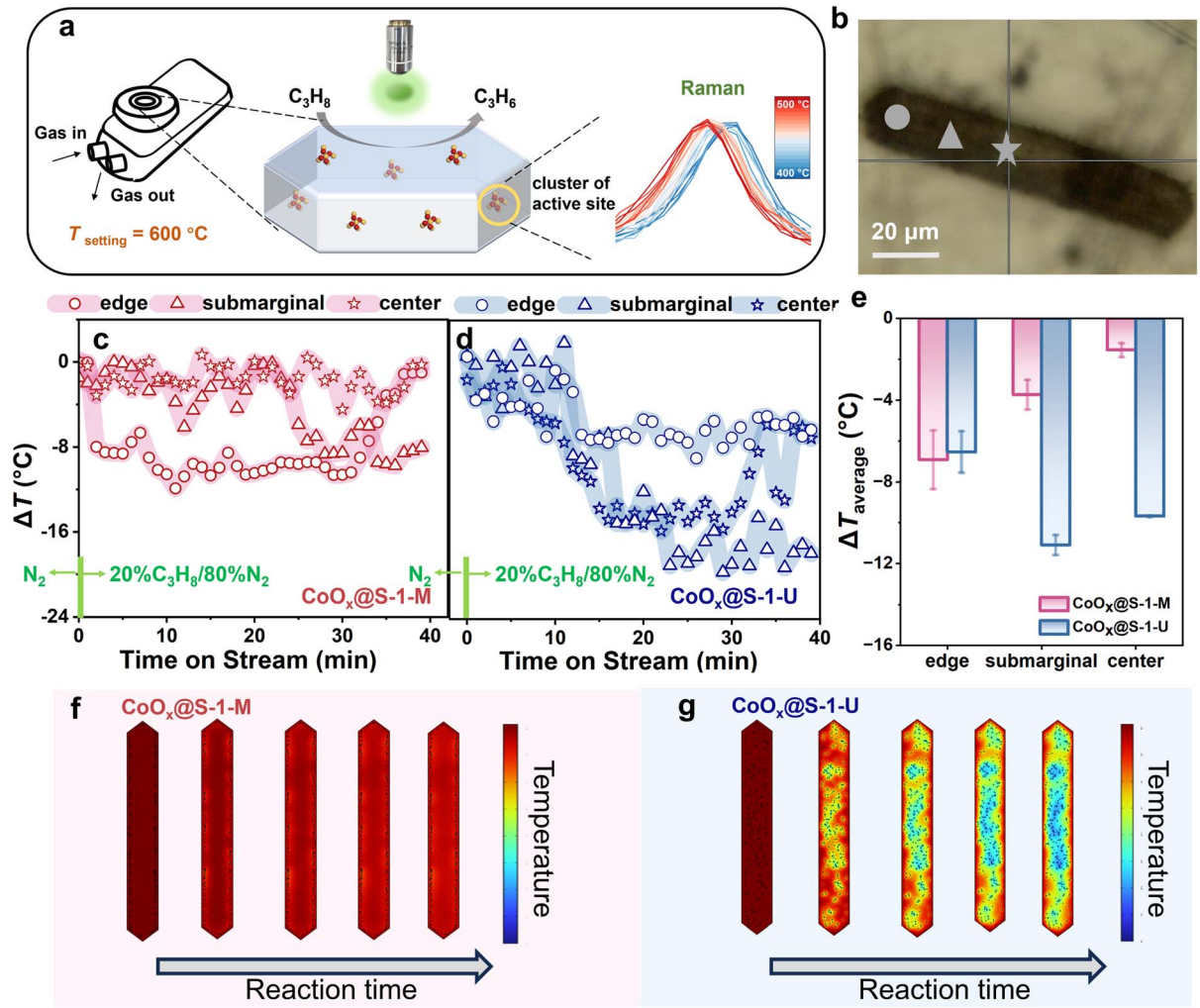

Fig. 5 *In situ* thermometry for metal oxide clusters in zeolites during the PDH reaction. (a) Catalysts were placed in an *in situ* cell, where individual zeolites were identified under a microscope. The temperature of a single crystal during the PDH reaction was determined by Raman thermometry. (b) Bright-field image of CoO_x@S-1 captured under HR-mRaman, marked with the edge (circle symbol), submarginal (triangle symbol), and center (five-pointed star symbol) locations of the crystal. Temperature drop across different locations of single crystals of (c) CoO_x@S-1-M and (d) CoO_x@S-1-U during the PDH reaction (the *in situ* cell was maintained at 575 °C, and ΔT denotes the temperature drop, $t = 0$ (switching from N_2 to propane)). (e) Comparisons of ΔT between the different locations of multiple crystals of CoO_x@S-1-M and CoO_x@S-1-U during the PDH reaction ($\Delta T_{average}$ denotes the mean ΔT recorded over the course of the PDH reaction, error bars represent the statistical dispersion (standard deviation) over $n = 6$ independent crystals). Simulations of the spatiotemporal temperature evolution of active CoO_x clusters in the (f) CoO_x@S-1-M and (g) CoO_x@S-1-U catalyst models during the endothermic PDH reaction (in the color bar, red corresponds to 575 °C and blue corresponds to 550 °C). Reaction conditions: feed gas of 20% C_3H_8 and 80% N_2; flow rate $F = 5$ ml min^{-1}; set temperature of the *in situ* cell $T = 575$ °C. Raman excitation wavelength: 532 nm, with a 20 s exposure time and a single cycle for each spectrum.

across different locations in a single CoO_x@S-1-M crystal during the PDH reaction. A slight temperature drop (~−9 °C) is observed at the edge of the CoO_x@S-1-M crystal, attributed to the active CoO_x clusters, which are located at the edge of the crystal during PDH. In contrast, almost no significant temperature drop can be observed at the submarginal (~−2 °C) and center (~−1 °C) regions of the CoO_x@S-1-M crystal due to the absence of active CoO_x clusters in these regions. As shown in Fig. 5d, compared to the temperature variations in CoO_x@S-1-M, the distinct spatiotemporal variations of temperature at active CoO_x clusters across different locations in a single CoO_x@S-1-U crystal can be observed. In the CoO_x@S-1-U crystals, where active CoO_x clusters are uniformly distributed within the crystal, the temperature drop of active CoO_x clusters in the interior (submarginal: ~−19 °C and center: ~−14 °C) of the crystal is greater than that at the edge of the crystal (~−8 °C). Fig. S20 and S21 show the time evolution of ΔT at different locations within multiple CoO_x@S-1-M and CoO_x@S-1-U crystals, respectively, and the observed trends are consistent with the ΔT distributions shown in Fig. 5c and d. Specifically, CoO_x@S-1-U exhibits a pronounced temperature gradient from the crystal edge toward the interior, whereas CoO_x@S-1-M maintains a relatively stable and more uniform internal temperature distribution. In addition, the temperature within CoO_x@S-1-U crystals remains lower than that within CoO_x@S-1-M crystals. Although the ΔT distribution trends are consistent

across multiple crystals, the absolute magnitude of ΔT shows some inter-crystal variation. Such variations can reasonably arise from differences in the actual crystal geometry and heat-conduction pathways, slight differences in the spatial distribution of CoO_x, and variations in the thermal boundary conditions between the crystal and the gas phase. The error bars in Fig. 5e (standard deviation, $n = 6$) further confirm that, although inter-crystal variation exists, it does not affect the overall temperature-distribution trend or the temperature differences between the two catalysts with distinct spatial distributions of CoO_x. These results also confirm the statistical robustness of the temperature measurements. Such differences in the temperature drop of active CoO_x clusters between CoO_x@S-1-M ($\sim$−6 °C, with 15% conversion of propane at initial temperature of 575 °C) and CoO_x@S-1-U ($\sim$−14 °C, with 10% conversion of propane at an initial temperature of 575 °C) provide a clear explanation for their distinct catalytic performances in the PDH reaction.

Fig. 5c and d also reflect the kinetic process of temperature-gradient development. At the initial stage after switching the feed gas, the reaction rate microscopically undergoes gas replacement, adsorption, activation, and then reaches a stable surface coverage. During this period, reaction-induced heat consumption occurs at the active CoO_x clusters, while heat replenishment is simultaneously provided by external hot-gas convection and heat conduction within the crystal, resulting in a nearly stable or slowly varying ΔT over a short time window. Subsequently, when the reaction within CoO_x@S-1-U enters a sustained stage, heat is continuously consumed inside the crystal, while heat replenishment is limited by the finite rate of heat conduction. This leads to a more pronounced temperature drop within the crystal and the gradual establishment of a temperature gradient decreasing from the crystal edge toward the center. In contrast, because the active CoO_x clusters in CoO_x@S-1-M are mainly located near the crystal edge, there is no sustained heat consumption in the crystal interior and the heat-transfer pathway is shorter. As a result, ΔT remains smaller, and the temperature field is more readily re-equilibrated.

To gain deeper mechanistic insight into the observed temperature distribution of active CoO_x clusters in the zeolites during the PDH reaction, we have performed additional simulations of the spatiotemporal temperature evolution in the CoO_x@S-1-U and CoO_x@S-1-M catalyst models. As shown in Fig. 5f and g, for the same zeolite support, the spatial distribution of active CoO_x clusters in CoO_x@S-1-U is relatively uniform, while that in CoO_x@S-1-M is close to the outer edge of the crystal. It was found that the temperature within CoO_x@S-1-M crystallites is relatively high and uniformly distributed, whereas CoO_x@S-1-U exhibits a lower internal temperature with a pronounced gradient that decreases from the crystal edge toward the center. Both CoO_x@S-1-M and CoO_x@S-1-U possess comparable overall thermal conductivity. However, for CoO_x@S-1-M, no significant endothermic reaction occurs within the zeolite, resulting in a stable internal temperature distribution. Under continuous external heating, efficient internal heat conduction enables rapid temperature re-equilibration inside the crystal. As a result, the edge regions can quickly compensate for local heat loss, maintaining overall thermal uniformity. In contrast, CoO_x@S-1-U undergoes continuous dehydrogenation reactions accompanied by substantial endothermic effects. During the reaction, local heat is continuously consumed, while the replenishment of heat from the external environment is limited by the intrinsic thermal conductivity. This imbalance leads to the formation of a temperature gradient within the crystal. As a result, under identical external heating conditions, the average internal temperature of CoO_x@S-1-U remains lower. Conventional catalyst designs are typically aimed to achieve a uniform distribution of active sites within the zeolite framework.[8] However, our findings reveal that for the exothermic reaction, the location of metal oxide catalysts at the edge of zeolite can effectively promote the catalytic performance of the PDH reaction by decreasing the temperature drop.

2.4 Mechanistic role of temperature in the stability of CoO_x@S-1 catalysts during the PDH reaction

To further elucidate the relationship between temperature of active CoO_x clusters and catalytic performance, FT-mIR spectroscopy using synchrotron infrared light was performed on single CoO_x@S-1. The PDH reaction was conducted within the *in situ* reaction cell positioned under an IR microscope, with the temperature set to 575 °C. Fig. S22 presents a bright-field image of CoO_x@S-1 zeolite under FT-mIR with the edge, submarginal, and center locations of the crystal, where the infrared spot was focused on a localized location. A series of IR spectra were recorded during the reaction (Fig. 6a). The absorption band observed at the 1500–2000 cm^{-1} range can be attributed to C=C stretching vibration, which indicates the formation of active intermediates such as olefins and aromatic species during the PDH reaction[50,57] (Fig. 6b). Both active-intermediate formation and propane conversion efficiency can be quantified by comparing integrated absorption peaks at the 1500–2000 cm^{-1} range. Fig. 6c and d compare the evolution of these active intermediates at different locations of active CoO_x clusters within CoO_x@S-1-M and CoO_x@S-1-U. A gradual build-up of the sp^2 C=C signal is observed during the reaction, followed by a tendency toward saturation. Notably, the overall intensity of the sp^2 C=C signal in CoO_x@S-1-M is higher than that in CoO_x@S-1-U, indicating a higher concentration of intermediates in CoO_x@S-1-M during PDH. This result is consistent with its higher local temperature and higher propane conversion, as shown in Fig. 5e. In addition, higher local temperature may further influence the formation and distribution of intermediates by accelerating their dehydrogenation or condensation and facilitating their desorption from active CoO_x clusters. As shown in Fig. S23, the correlation between the temperatures of active CoO_x clusters at different locations and the concentrations of active intermediates within CoO_x@S-1 zeolites further indicates that higher local temperatures promote intermediate formation and thus facilitate propane conversion.

More comprehensive characterization studies of the coke species formed in CoO_x@S-1-U and CoO_x@S-1-M after exposure

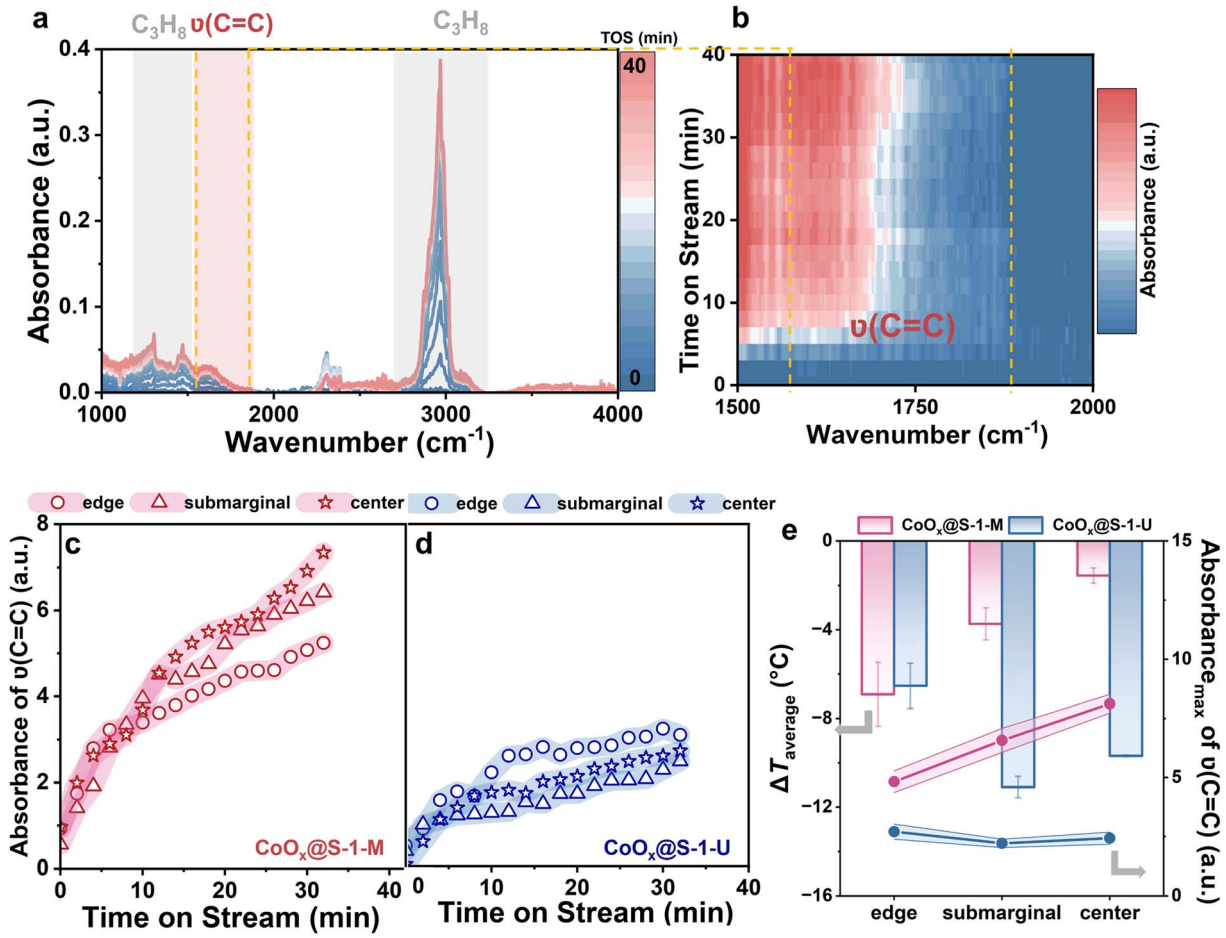

Fig. 6 Characterization of active-intermediates at different locations of zeolites. (a) *In situ* FT-mIR of CoO_x@S-1-M during the PDH reaction and (b) the absorbance of the absorption peak corresponding to the sp^2-hybridized C=C stretching vibrations (1500–2000 cm^{-1}). Reaction conditions: feed gas of 20% C_3H_8 and 80% N_2; flow rate $F = 5$ ml min^{-1}; set temperature in the reaction cell $T = 575$ °C. Comparison of absorbance peaks (1500–2000 cm^{-1}) of active-intermediates for (c) CoO_x@S-1-M and (d) CoO_x@S-1-U, along with the distribution of active-intermediates across different locations of single crystals during the PDH reaction. (e) Relationship between local temperature of active clusters and the concentration of active intermediates during the PDH reaction ($Absorbance_{max}$ represents the maximum absorbance of active intermediates).

to propane for 20 h were performed using temperature-programmed oxidation (TPO), PL and MALDI FT-ICR MS, as shown in Fig. 7. The TPO profiles, presented as CO_2/Ar MS signals (Fig. 7a), reveal that CoO_x@S-1-U exhibits a broader CO_2 evolution peak compared with CoO_x@S-1-M, suggesting the presence of more diverse coke species. The maximum CO_2 evolution temperature (T_{max}-CO_2) for CoO_x@S-1-M is 600 °C, whereas that for CoO_x@S-1-U is 650 °C, implying that larger and more thermally stable coke species are formed within the CoO_x@S-1-U zeolite. PL spectra further provide insight into the nature of coke species (Fig. 7b). For CoO_x@S-1-M, a single PL band appears at 650 nm, corresponding to the π–π* transitions of coke.[62] In contrast, CoO_x@S-1-U exhibits two PL bands at 650 nm and 700 nm, indicative of the formation of heavier and more conjugated coke species than those present in CoO_x@S-1-M. The generation of these heavier coke species within CoO_x@S-1-U explains its larger k_d value and greater tendency toward deactivation. MALDI FT-ICR MS was employed to analyze the molecular characteristics of coke species extracted from the catalysts after 20 h of reaction (Fig. 7c and Table S8). The spectra of coke species, extracted using CCl_4 from HF-dissolved samples, exhibit ion clusters distributed across m/z ranges of 230–410, 600–650, 920–1200, and 1350–1500 Da (the calculation of coke homologous series is detailed in Section S6 of the SI).[63] The relative intensity of coke-related peaks in CoO_x@S-1-U, normalized to the internal standard peak (m/z = 227 Da), is higher than that in CoO_x@S-1-M, indicating the formation of a larger quantity of coke species with similar mass-to-charge ratios. Moreover, the presence of a greater number of peaks within the same homologous series in CoO_x@S-1-U suggests a higher diversity of coke species and more extensive carbon-chain growth. This observation is consistent with the theoretical calculation.

Given that the adsorption of propylene on active CoO_x clusters facilitates side reactions leading to coke formation, periodic DFT and MD simulations[64] were performed to evaluate the adsorption probability of propylene in the temperature range of 550–650 °C. As shown in Fig. 8a and S24, after C–H bond

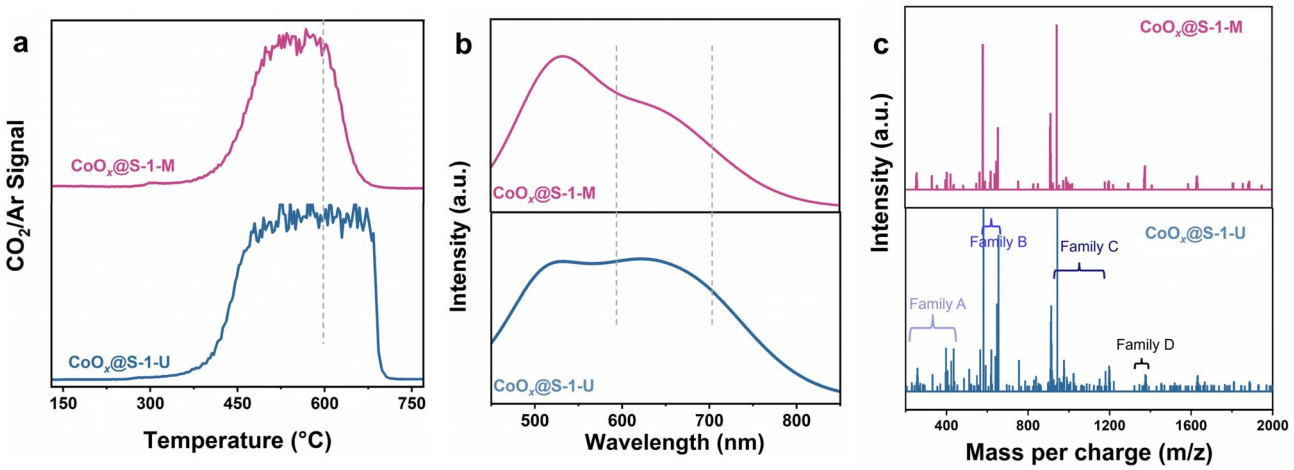

Fig. 7 Characterization of coke species in deactivated catalysts. (a) TPO profiles, (b) PL spectra and (c) MALDI FT-ICR mass spectra of CoO_x@S-1-U and CoO_x@S-1-M after exposure to propane for 20 h. PL measurement conditions: excitation wavelength is 325 nm; grating resolution is 100 grooves per mm.

activation of adsorbed propane on active CoO_x clusters occurs, propylene and two H* atoms are formed. Then, the propylene desorbs, while H_2 is formed from the two H* atoms. However, it can be noticed that after the formation of H_2 on the active CoO_x clusters, the propylene is preferentially adsorbed on active CoO_x clusters due to the thermodynamic advantage. In addition, the activation energy of propylene dehydrogenation is relative lower ($\sim$80.8 kJ mol^{-1}) compared to the overall pathway. According to the Arrhenius equation, this illustrates that the rate of propylene dehydrogenation is not particularly sensitive to temperature at the high temperatures of 823–923 K. Therefore, reducing the adsorption probability of propylene on the active CoO_x clusters can mitigate the coke formation. The adsorption of propylene on active CoO_x clusters at 823–923 K was performed by the MD simulations. As shown in Fig. 8b and c, it can be observed that as the temperature increases, the adsorption probability of propylene on active CoO_x clusters significantly reduces. Therefore, properly elevating the local temperature can be beneficial to reduce the coke formation on active CoO_x clusters. Integrating the experimental and computational results, we conclude that the higher local temperature of CoO_x@S-1-M promote propylene desorption and hinder coke

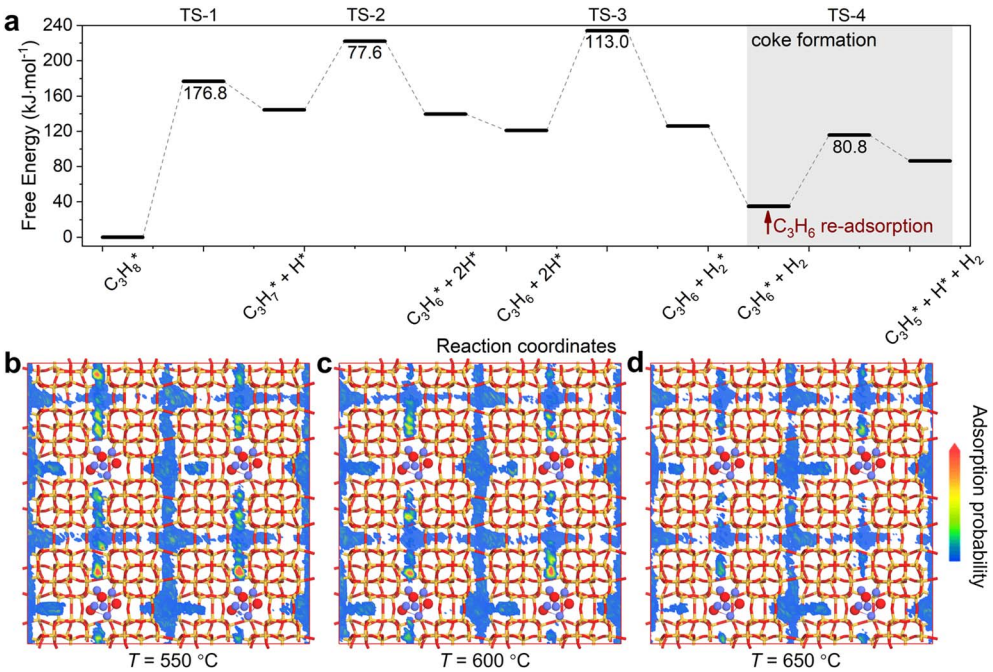

Fig. 8 (a) Energy profiles for dehydrogenation of propane to propylene and coke precursors and H_2 formation on active CoO_x clusters in the channels of S-1. MD simulations of the adsorption probability of propylene on active CoO_x sites within S-1 channels at reaction temperatures of (b) 550, (c) 600, and (d) 650 °C. Orange, red, and violet spheres represent Si, O, and Co atoms, respectively.

formation, leading to enhanced catalytic activity and stability during PDH. This behavior is inconsistent with the commonly accepted notion that higher temperatures generally promote the growth of coke species, and thus represents a new and intriguing phenomenon. Consequently, the CoO_x@S-1-M catalyst, which exhibits a higher local temperature during the PDH reaction, demonstrates enhanced structural stability and resistance to deactivation.

3. Conclusion

In heterogeneous catalysis, the nature of active sites fundamentally governs catalytic behavior; however, despite extensive efforts devoted to structural design, the influence of local temperature gradients surrounding these sites within solid catalysts has remained largely unexplored. In this work, we conclude that PDH activity and stability are enhanced when CoO_x is peripherally confined near the surface of S-1 crystals (CoO_x@S-1-M), rather than following the conventional catalyst design strategy of uniformly dispersing active species within the support (CoO_x@S-1-U) to achieve high stability. HR-mRaman spectroscopy reveals that CoO_x@S-1-M experiences a smaller temperature drop than CoO_x@S-1-U. While CoO_x@S-1-U develops a pronounced temperature gradient within the zeolite, with a core-to-edge temperature difference exceeding 17 °C, CoO_x@S-1-M maintains a much more uniform temperature distribution, with the difference limited to 8 °C. As a consequence, CoO_x@S-1-M consistently exhibits higher propane conversion in the range of 500–600 °C and an ~30% lower deactivation rate constant compared with CoO_x@S-1-U, demonstrating superior catalytic stability. Experimental coke characterization combined with theoretical analysis clarifies the mechanistic role of temperature in governing the catalytic stability of CoO_x@S-1 catalysts during PDH. The results show that the smaller temperature drop at active CoO_x clusters in CoO_x@S-1-M promotes propylene desorption and suppresses side reactions and coke formation, in contrast to the commonly accepted view that higher temperatures generally favor coke growth. This finding clearly elucidates the impact of local heat generation and transfer at active clusters on catalytic performance arising from the spatial distribution of the active clusters. Therefore, it is important to understand the mechanisms of heterogeneous catalysis from the perspective of heat management at active clusters, which will offer new guidance for the rational design of solid catalysts such as zeolite-supported metal catalysts with enhanced catalytic performance.

Author contributions

B. Z., M. B. G. and M. Y. initiated the project, led the project and wrote the manuscript. Z. K. X., H. B. Z. and B. Z. prepared the catalysts and performed the catalyst characterization. B. Z. and M. B. G. carried out the *in situ* Raman thermometry experiments. B. Z., G. D. L. and H. C. conducted the fixed-bed reactor tests for propane dehydrogenation. D. Z. contributed to the analysis of the propane dehydrogenation reaction. B. Z. and G. M. processed the *in situ* Raman spectra and organized the temperature-measurement data. B. Z. and T. Z. performed the photoluminescence spectroscopy measurements. M. B. G. carried out the simulations.

Conflicts of interest

There are no conflicts to declare.

Data availability

The data supporting this study are available from the corresponding author upon reasonable request.

Supplementary information (SI): details of the experimental procedures and theoretical simulations are provided in the SI Appendix. The methods for the preparation of S-1 zeolites and the synthesis of CoO_x@S-1 catalysts with different spatial distributions of active CoO_x clusters are described in the SI Appendix, Catalyst preparation. The detailed characterization procedures for CoO_x@S-1 catalysts (including XRD, MAS NMR, ICP-OES, nitrogen physisorption, XAS, TOF-SIMS, O_2-TPO, DR UV-vis, MALDI FT-ICR MS, XPS, and IGA) are provided in the SI Appendix, Characterizations. The procedures for *in situ* spectroscopic measurements (*in situ* Raman thermometry, *in situ* FT-mIR spectroscopy, and PL imaging) are described in the SI Appendix, Experiments. The methods for PDH catalytic tests, catalyst performance evaluation, and the assessment of internal and external diffusion effects are provided in the SI Appendix, Experiments and Tables S4–S6. Theoretical simulation details, including periodic *ab initio* static simulations and Monte Carlo simulations, are described in the SI Appendix, Theoretical simulations. Supporting data, including catalyst characterization results (Table S1), fitting parameters of *in situ* XAFS spectra (Tables S2 and S7), equilibrium conversions (Table S3), IGA fitting results and diffusion-related parameter calculations (Tables S4–S6), and the families of coke species (Table S8), can also be found in the SI Appendix. See DOI: https://doi.org/10.1039/d6sc01014h.

Acknowledgements

The authors are thankful for the financial support from the National Natural Science Foundation of China, China (Grant No. 22293021, 22288101, 22494712 and 22208337). The authors also thank Dr Shuwen Yu at the Dalian Institute of Chemical Physics for helpful discussion on Raman spectra, Dr Dan Zhao at the Dalian Institute of Chemical Physics for valuable suggestions regarding propylene desorption, Dr Hua Li at the Dalian Institute of Chemical Physics for helpful guidance on heat transfer, Mr Wenguang Yu at the Dalian Institute of Chemical Physics for his assistance with IGA measurements, Mr Yuhan Song and Mr Yu Tian at the Dalian Institute of Chemical Physics for their assistance with fixed-bed experiments, Dr Jingfeng Han at the Dalian Institute of Chemical Physics for helpful discussion about IR, Dr Yang Yu at the Dalian Institute of Chemical Physics for helpful experiments on TOF-SIMS, Dr Li Wang at the Dalian Institute of Chemical Physics for valuable discussions on homologous series analysis, Ms Yuli Liu at the

Dalian Institute of Chemical Physics for the kind discussion about PL spectra, and Ms Yanli He at the Dalian Institute of Chemical Physics for the kind discussion about nitrogen adsorption–desorption isotherms. The authors thank the staff of the BL06B, BL11B and BL20U beamline at the Shanghai Synchrotron Radiation Facility (SSRF) for assistance during the *in situ* mIR experiment.

References

1 L. Liu, M. Lopez-Haro, C. W. Lopes, C. Li, P. Concepcion, L. Simonelli, J. J. Calvino and A. Corma, Regioselective generation and reactivity control of subnanometric platinum clusters in zeolites for high-temperature catalysis, *Nat. Mater.*, 2019, **18**, 866–873.

2 R. Ryoo, J. Kim, C. Jo, S. W. Han, J.-C. Kim, H. Park, J. Han, H. S. Shin and J. W. Shin, Rare-earth–platinum alloy nanoparticles in mesoporous zeolite for catalysis, *Nature*, 2020, **585**, 221–224.

3 Y. Chai, G. Wu, X. Liu, Y. Ren, W. Dai, C. Wang, Z. Xie, N. Guan and L. Li, Acetylene-Selective Hydrogenation Catalyzed by Cationic Nickel Confined in Zeolite, *J. Am. Chem. Soc.*, 2019, **141**, 9920–9927.

4 J. Zhong, Y. Xu and Z. Liu, Heterogeneous non-mercury catalysts for acetylene hydrochlorination: progress, challenges, and opportunities, *Green Chem.*, 2018, **20**, 2412–2427.

5 N. Blanch-Raga, A. E. Palomares, J. Martínez-Triguero and S. Valencia, Cu and Co modified beta zeolite catalysts for the trichloroethylene oxidation, *Appl. Catal., B*, 2016, **187**, 90–97.

6 Z. Jin, L. Wang, E. Zuidema, K. Mondal, M. Zhang, J. Zhang, C. Wang, X. Meng, H. Yang, C. Mesters and F.-S. Xiao, Hydrophobic zeolite modification for in situ peroxide formation in methane oxidation to methanol, *Science*, 2020, **367**, 193–197.

7 H. Zhou, X. Yi, Y. Hui, L. Wang, W. Chen, Y. Qin, M. Wang, J. Ma, X. Chu, Y. Wang, X. Hong, Z. Chen, X. Meng, H. Wang, Q. Zhu, L. Song, A. Zheng and F.-S. Xiao, Isolated boron in zeolite for oxidative dehydrogenation of propane, *Science*, 2021, **372**, 76–80.

8 Q. Zhang, S. Gao and J. Yu, Metal Sites in Zeolites: Synthesis, Characterization, and Catalysis, *Chem. Rev.*, 2022, **123**, 6039–6106.

9 M. Cargnello, V. V. T. Doan-Nguyen, T. R. Gordon, R. E. Diaz, E. A. Stach, R. J. Gorte, P. Fornasiero and C. B. Murray, Control of Metal Nanocrystal Size Reveals Metal-Support Interface Role for Ceria Catalysts, *Science*, 2013, **341**, 771–773.

10 P. Rzepka, T. Huthwelker, J. Dedecek, E. Tabor, M. Bernauer, S. Sklenak, K. Mlekodaj and J. A. van Bokhoven, Aluminum distribution and active site locations in the structures of zeolite ZSM-5 catalysts, *Science*, 2025, **388**, 423–428.

11 X. Tang, Z. Liu, L. Huang, W. Chen, C. Li, G. Wang, G. Li, X. Yi and A. Zheng, Violation or Abidance of Löwenstein's Rule in Zeolites under Synthesis Conditions?, *ACS Catal.*, 2019, **9**, 10618–10625.

12 K. Cheng, L. C. J. Smulders, L. I. van der Wal, J. Oenema, J. D. Meeldijk, N. L. Visser, G. Sunley, T. Roberts, Z. Xu, E. Doskocil, H. Yoshida, Y. Zheng, J. Zečević, P. E. de Jongh and K. P. de Jong, Maximizing noble metal utilization in solid catalysts by control of nanoparticle location, *Science*, 2022, **377**, 204–208.

13 T. S. Jacobs, T. P. van Swieten, S. J. W. Vonk, I. P. Bosman, A. E. M. Melcherts, B. C. Janssen, J. C. L. Janssens, M. Monai, A. Meijerink, F. T. Rabouw, W. van der Stam and B. M. Weckhuysen, Mapping Temperature Heterogeneities during Catalytic CO_2 Methanation with Operando Luminescence Thermometry, *ACS Nano*, 2023, **17**, 20053–20061.

14 I. L. C. Buurmans and B. M. Weckhuysen, Heterogeneities of individual catalyst particles in space and time as monitored by spectroscopy, *Nat. Chem.*, 2012, **4**, 873–886.

15 Y. Shang, Q. Han, S. Hao, T. Chen, Y. Zhu, Z. Wang and C. Yang, Dual-Mode Upconversion Nanoprobe Enables Broad-Range Thermometry from Cryogenic to Room Temperature, *ACS Appl. Mater. Interfaces*, 2019, **11**, 42455–42461.

16 W. Piotrowski, L. Dalipi, K. Elzbieciak-Piecka, A. Bednarkiewicz, B. Fond and L. Marciniak, Self-Referenced Temperature Imaging with Dual Light Emitting Diode Excitation and Single-Band Emission of AVO_4:Eu^{3+} (A = Y, La, Lu, Gd) Nanophosphors, *Adv. Photonics Res.*, 2022, **3**, 2100139.

17 J. C. Saint Remi, A. Lauerer, C. Chmelik, I. Vandendael, H. Terryn, G. V. Baron, J. F. Denayer and J. Karger, The role of crystal diversity in understanding mass transfer in nanoporous materials, *Nat. Mater.*, 2016, **15**, 401–406.

18 J. Kärger, T. Binder, C. Chmelik, F. Hibbe, H. Krautscheid, R. Krishna and J. Weitkamp, Microimaging of transient guest profiles to monitor mass transfer in nanoporous materials, *Nat. Mater.*, 2014, **13**, 333–343.

19 A. N. Parvulescu, D. Mores, E. Stavitski, C. M. Teodorescu, P. C. A. Bruijnincx, R. J. M. K. Gebbink and B. M. Weckhuysen, Chemical Imaging of Catalyst Deactivation during the Conversion of Renewables at the Single Particle Level: Etherification of Biomass-Based Polyols with Alkenes over H-Beta Zeolites, *J. Am. Chem. Soc.*, 2010, **132**, 10429–10439.

20 S. Hwang and R. Smith, Optimum Reactor Design in Methanation Processes with Nonuniform Catalysts, *Chem. Eng. Commun.*, 2008, **196**, 616–642.

21 E. Borodina, F. Meirer, I. Lezcano-González, M. Mokhtar, A. M. Asiri, S. A. Al-Thabaiti, S. N. Basahel, J. Ruiz-Martinez and B. M. Weckhuysen, Influence of the Reaction Temperature on the Nature of the Active and Deactivating Species during Methanol to Olefins Conversion over H-SSZ-13, *ACS Catal.*, 2015, **5**, 992–1003.

22 I. C. Medeiros-Costa, E. Dib, N. Nesterenko, J. P. Dath, J. P. Gilson and S. Mintova, Silanol defect engineering and healing in zeolites: opportunities to fine-tune their properties and performances, *Chem. Soc. Rev.*, 2021, **50**, 11156–11179.

23 J. A. Dumesic, G. W. Huber and M. Boudart, in *Handbook of Heterogeneous Catalysis*, 1996, DOI: 10.1002/9783527610044.hetcat0001.
24 J. K. Nørskov, T. Bligaard, B. Hvolbæk, F. Abild-Pedersen, I. Chorkendorff and C. H. Christensen, The nature of the active site in heterogeneous metal catalysis, *Chem. Soc. Rev.*, 2008, **37**, 2163–2171.
25 G. B. Marin, G. S. Yablonsky and D. Constales, In *Kinetics of Chemical Reactions*, 2019, pp. 263–305, DOI: DOI: 10.1002/9783527808397.ch9.
26 Z. Lian, C. Si, F. Jan, S. Zhi and B. Li, Coke Deposition on Pt-Based Catalysts in Propane Direct Dehydrogenation: Kinetics, Suppression, and Elimination, *ACS Catal.*, 2021, **11**, 9279–9292.
27 C. Chen, S. Zhang, Z. Wang and Z.-Y. Yuan, Ultrasmall Co confined in the silanols of dealuminated beta zeolite: a highly active and selective catalyst for direct dehydrogenation of propane to propylene, *J. Catal.*, 2020, **383**, 77–87.
28 Z. Li, S. Chen, W. Wang, J. Sun, X. Wang, D. Fu, Z.-J. Zhao, C. Pei and J. Gong, Proximity-Dependent Oxide–Support Interactions in Cobalt/Ceria-Based Catalysts for Propane Dehydrogenation, *ACS Catal.*, 2025, **15**, 6078–6087.
29 S. Chen, Y. Xu, X. Chang, Y. Pan, G. Sun, X. Wang, D. Fu, C. Pei, Z.-J. Zhao, D. Su and J. Gong, Defective TiO_x overlayers catalyze propane dehydrogenation promoted by base metals, *Science*, 2024, **385**, 295–300.
30 M. Simeone, L. Salemme, C. Allouis and G. Volpicelli, Temperature profile in a reverse flow reactor for catalytic partial oxidation of methane by fast IR imaging, *AIChE J.*, 2008, **54**, 2689–2698.
31 I. V. Koptyug, A. V. Khomichev, A. A. Lysova and R. Z. Sagdeev, Spatially Resolved NMR Thermometry of an Operating Fixed-Bed Catalytic Reactor, *J. Am. Chem. Soc.*, 2008, **130**, 10452–10453.
32 L. Mascaretti, A. Schirato, T. Montini, A. Alabastri, A. Naldoni and P. Fornasiero, Challenges in temperature measurements in gas-phase photothermal catalysis, *Joule*, 2022, **6**, 1727–1732.
33 T. Hartman, R. G. Geitenbeek, G. T. Whiting and B. M. Weckhuysen, Operando monitoring of temperature and active species at the single catalyst particle level, *Nat. Catal.*, 2019, **2**, 986–996.
34 T. Hartman, R. G. Geitenbeek, C. S. Wondergem, W. van der Stam and B. M. Weckhuysen, Operando Nanoscale Sensors in Catalysis: All Eyes on Catalyst Particles, *ACS Nano*, 2020, **14**, 3725–3735.
35 Y. Tian, M. Gao, H. Xie, S. Xu, M. Ye and Z. Liu, Spatiotemporal Heterogeneity of Temperature and Catalytic Activation within Individual Catalyst Particles, *J. Am. Chem. Soc.*, 2024, **146**, 4958–4972.
36 M. Filez, V. De Coster, H. Poelman, V. Briois, A. Beauvois, J. Dendooven, M. B. J. Roeffaers, V. Galvita and C. Detavernier, Selectively monitoring the operando temperature of active metal nanoparticles during catalytic reactions by X-ray absorption nanothermometry, *Nat. Catal.*, 2025, **8**, 187–195.
37 R. Vogel, D. W. Groefsema, M. A. van den Bulk, T. S. Jacobs, P. T. Prins, F. T. Rabouw and B. M. Weckhuysen, Operando Luminescence Thermometry for Hydrocarbon Conversion Catalysis: Dealing with Dynamic Changes in Catalyst Optical Properties, *ACS Appl. Mater. Interfaces*, 2025, **17**, 21215–21222.
38 R. C. Elias, B. Yan and S. Linic, Probing Spatial Energy Flow in Plasmonic Catalysts from Charge Excitation to Heating: Nonhomogeneous Energy Distribution as a Fundamental Feature of Plasmonic Chemistry, *J. Am. Chem. Soc.*, 2024, **146**, 29656–29663.
39 G. Wang, X. Zhu and C. Li, Recent Progress in Commercial and Novel Catalysts for Catalytic Dehydrogenation of Light Alkanes, *Chem. Rec.*, 2019, **20**, 604–616.
40 J. J. H. B. Sattler, J. Ruiz-Martinez, E. Santillan-Jimenez and B. M. Weckhuysen, Catalytic Dehydrogenation of Light Alkanes on Metals and Metal Oxides, *Chem. Rev.*, 2014, **114**, 10613–10653.
41 S. Chen, X. Chang, G. Sun, T. Zhang, Y. Xu, Y. Wang, C. Pei and J. Gong, Propane dehydrogenation: catalyst development, new chemistry, and emerging technologies, *Chem. Soc. Rev.*, 2021, **50**, 3315–3354.
42 Z. Qu and Q. Sun, Advances in zeolite-supported metal catalysts for propane dehydrogenation, *Inorg. Chem. Front.*, 2022, **9**, 3095–3115.
43 J. Liu, J. Wang, Y. Zhang, W. Zheng, Y. Yao, Q. Liu, X. Zhang, Y. Yang and X. Wang, Improved C–H Activation in Propane Dehydrogenation Using Zeolite-Stabilized Co–O Moieties, *ACS Catal.*, 2023, **13**, 14737–14745.
44 J. Grand, S. N. Talapaneni, A. Vicente, C. Fernandez, E. Dib, H. A. Aleksandrov, G. N. Vayssilov, R. Retoux, P. Boullay, J.-P. Gilson, V. Valtchev and S. Mintova, One-pot synthesis of silanol-free nanosized MFI zeolite, *Nat. Mater.*, 2017, **16**, 1010–1015.
45 Y. Hou, C. Zhu, H. Sun, Y. Zhao, S. Pan, S. Ma, Q. Fu, X. Sui, X. Liu, L. Jiang and J. Gao, Artificial Cation-Chloride Co-Transporters for Chloride-Facilitated Lithium/Magnesium Separation, *Angew Chem. Int. Ed. Engl.*, 2025, e202504259, DOI: 10.1002/anie.202504259.
46 X. Yang, E. Dib, Q. Lang, H. Guo, G. Fu, J. Wang, Q. Yi, H. Zhao and V. Valtchev, Silicalite-1 formation in acidic medium: synthesis conditions and physicochemical properties, *Microporous Mesoporous Mater.*, 2022, **329**, 111537.
47 P. Liu, Q.-H. Zhang, J.-Q. Zhang, J.-M. Hu and F.-H. Cao, Rapid synthesis of highly oriented hydrophobic silicalite-1 zeolite films on alloy steel at lower temperature for corrosion protection, *Chem. Eng. J.*, 2022, **430**, 133173.
48 T. Jiang, W. Shen, Q. Zhao, M. Li, J. Chu and H. Yin, Characterization of CoMCM-41 mesoporous molecular sieves obtained by the microwave irradiation method, *J. Solid State Chem.*, 2008, **181**, 2298–2305.
49 K. Tang and X. Hong, Preparation and Characterization of Co–MCM-41 and Its Adsorption Removing Basic Nitrogen Compounds from Fluidized Catalytic Cracking Diesel Oil, *Energy Fuels*, 2016, **30**, 4619–4624.

50 Z.-P. Hu, G. Qin, J. Han, W. Zhang, N. Wang, Y. Zheng, Q. Jiang, T. Ji, Z.-Y. Yuan, J. Xiao, Y. Wei and Z. Liu, Atomic Insight into the Local Structure and Microenvironment of Isolated Co-Motifs in MFI Zeolite Frameworks for Propane Dehydrogenation, *J. Am. Chem. Soc.*, 2022, **144**, 12127–12137.

51 Z. Xu, M. Gao, Y. Wei, Y. Yue, Z. Bai, P. Yuan, P. Fornasiero, J.-M. Basset, B. Mei, Z. Liu, H. Zhu, M. Ye and X. Bao, Pt migration–lockup in zeolite for stable propane dehydrogenation catalyst, *Nature*, 2025, **643**, 691–698.

52 M. Hartmann, A. G. Machoke and W. Schwieger, Catalytic test reactions for the evaluation of hierarchical zeolites, *Chem. Soc. Rev.*, 2016, **45**, 3313–3330.

53 Z. Zang, Y. Ren, C. Fan, Y. Cheng, L. Li, X. Yu, X. Yang, Z. Lu, X. Zhang and H. Liu, Constructing unsaturated coordination Co–M (M = P, S, Se, Te) bonds modified metallic Co for efficient alkaline hydrogen evolution, *Appl. Catal. B Environ. Energy*, 2024, **350**, 123912.

54 Y. Du, F. Xie, M. Lu, R. Lv, W. Liu, Y. Yan, S. Yan and Z. Zou, Continuous strain tuning of oxygen evolution catalysts with anisotropic thermal expansion, *Nat. Commun.*, 2024, **15**, 1780.

55 L. Liu, H. Li, H. Zhou, S. Chu, L. Liu, Z. Feng, X. Qin, J. Qi, J. Hou, Q. Wu, H. Li, X. Liu, L. Chen, J. Xiao, L. Wang and F.-S. Xiao, Rivet of cobalt in siliceous zeolite for catalytic ethane dehydrogenation, *Chem*, 2023, **9**, 637–649.

56 Y. Yan, Z. Zhang, S.-M. Bak, S. Yao, X. Hu, Z. Shadike, C.-L. Do-Thanh, F. Zhang, H. Chen, X. Lyu, K. Chen, Y. Zhu, X. Lu, P. Ouyang, J. Fu and S. Dai, Confinement of Ultrasmall Cobalt Oxide Clusters within Silicalite-1 Crystals for Efficient Conversion of Fructose into Methyl Lactate, *ACS Catal.*, 2019, **9**, 1923–1930.

57 M. O. Guerrero-Pérez and M. A. Bañares, From conventional in situ to operando studies in Raman spectroscopy, *Catal. Today*, 2006, **113**, 48–57.

58 R. Koirala, O. V. Safonova, S. E. Pratsinis and A. Baiker, Effect of cobalt loading on structure and catalytic behavior of CoO_x/SiO_2 in CO_2-assisted dehydrogenation of ethane, *Appl. Catal., A*, 2018, **552**, 77–85.

59 A. Martinelli, S. Creci, S. Vavra, P. A. Carlsson and M. Skoglundh, Local anisotropy in single crystals of zeotypes with the MFI framework structure evidenced by polarised Raman spectroscopy, *Phys. Chem. Chem. Phys.*, 2020, **22**, 1640–1654.

60 J. Wang, J. L. You, A. A. Sobol, L. M. Lu, M. Wang, J. Wu, X. M. Lv and S. M. Wan, In-situ high temperature Raman spectroscopic study on the structural evolution of $Na_2W_2O_7$ from the crystalline to molten states, *J. Raman Spectrosc.*, 2017, **48**, 298–304.

61 H. Hong, S. Guo, L. Jin, Y. Mao, Y. Chen, J. Gu, S. Chen, X. Huang, Y. Guan, X. Li, Y. Li, X. Lü and Y. Fu, Two-dimensional lead halide perovskite lateral homojunctions enabled by phase pinning, *Nat. Commun.*, 2024, **15**, 3164.

62 S. Lee and M. Choi, Unveiling coke formation mechanism in MFI zeolites during methanol-to-hydrocarbons conversion, *J. Catal.*, 2019, **375**, 183–192.

63 N. Wang, Y. Zhi, Y. Wei, W. Zhang, Z. Liu, J. Huang, T. Sun, S. Xu, S. Lin, Y. He, A. Zheng and Z. Liu, Molecular elucidating of an unusual growth mechanism for polycyclic aromatic hydrocarbons in confined space, *Nat. Commun.*, 2020, **11**, 1079.

64 Y. Zhang, T. Yang, J. Hu, L. Wang, M. Gao, L. Qi, A. T. Bell, P. Tian and Z. Liu, Identification of Highly Active Co–O–Zn Sites in Silanol Nests for n-Butane Cascade Dehydrogenation to 1,3-Butadiene, *J. Am. Chem. Soc.*, 2025, **147**, 42110–42122.